

# Nonequilibrium plastic roughening of metallic glasses yields self-affine topographies with strain-rate and temperature-dependent scaling exponents

Wolfram G. Nöhring,<sup>1</sup> Adam R. Hinkle,<sup>2,3,4</sup> and Lars Pastewka<sup>1,2,5</sup>

<sup>1</sup>*Department of Microsystems Engineering,  
University of Freiburg, 79110 Freiburg, Germany*

<sup>2</sup>*Institute for Applied Materials, Karlsruhe  
Institute of Technology, 76131 Karlsruhe, Germany*

<sup>3</sup>*DCS Corporation, Belcamp, MD 21017, USA*

<sup>4</sup>*U.S. Army Combat Capabilities Development Command,  
Chemical and Biological Center, Aberdeen Proving Ground, MD 21010-5424, USA*

<sup>5</sup>*Cluster of Excellence livMatS, Freiburg Center for  
Interactive Materials and Bioinspired Technologies,  
University of Freiburg, 79110 Freiburg, Germany*

(Dated: January 11, 2022)

## Abstract

We study nonequilibrium roughening during compressive plastic flow of initially flat  $\text{Cu}_{50}\text{Zr}_{50}$  metallic glass using large-scale molecular dynamics simulations. Roughness emerges at atomically flat interfaces beyond the yield point of the glass. A self-affine rough topography is imprinted at yield and is reinforced during subsequent deformation. The imprinted topographies have Hurst exponents that decrease with increasing strain-rate and temperature. After yield, the root-mean-square roughness amplitude grows as the square-root of the applied strain with a prefactor that also drops with increasing strain-rate and temperature. Our calculations reveal the emergence of spatial power-law correlations from homogeneous samples during plastic flow with exponents that depend on the rate of deformation and the temperature. The results have implications for interpreting and engineering roughness profiles.

Roughness controls many interfacial phenomena. The most prominent examples are arguably the influence of roughness on friction [1, 2] and adhesion [3–8]. It is therefore useful to characterize surface roughness, and to understand the mechanisms that produce it, including growth, erosion, and fracture. Here, we focus on plastic deformation as a roughening mechanism: When a solid is deformed irreversibly by external forces, a signature of the deformation process is imprinted on the surface. For example, crystal dislocations in metals [9–13] or shear bands and fractures in rocks [14] leave slip traces behind that roughen surfaces.

Unlike crystalline metals, the fundamental deformation event in glasses is not a slip trace but a localized shear transformation or STZ (shear transformation zone) [15–18]. At low temperature (or slow deformation), these can coalesce to form deformation avalanches that potentially span the size of the whole system [19, 20]. Despite the importance of glasses for engineering applications and the wide interest in deformation of glasses in physics, little is known about the nonequilibrium processes forming their surface morphology.

Glasses formed by quenching have surfaces that are well described by capillary waves [21–23]. However, many natural and industrially processed surfaces are found to be self-affine fractals with power-law scaling of heights [24–29]. The root mean square (rms) amplitude of surface height fluctuations,  $h_{\text{rms}}(L)$ , measured in a square region with side of length  $L$ , then scales as  $h_{\text{rms}}(L) \propto L^H$  where  $H$  is the Hurst exponent.

Recent simulation studies have shown that deformation is one possible origin of self-affinity. For example, Milanese et al. [30] have observed self-affine roughening in 2D discrete-element simulations of sliding contacts that formed abrasive third bodies. We have recently shown using molecular-dynamics calculations that self-affine roughness emerges naturally during compression of atomically flat surfaces made from pure metals, crystalline alloys, and metallic glasses [13]. Similar results have been obtained by Vacher & de Wijn for the surface of polymers [31].

We here present evidence that – unlike in crystalline materials [13] – the roughness characteristics of a glass depend strongly on temperature and deformation rate. We show that two regimes of temperature and strain rate must be distinguished. In quasi-static deformation, and at the lowest temperatures and rates, the topography is dominated by system-spanning shear bands. Self-affine scaling of surface heights is nevertheless plausible through a mechanism similar to slip of crystal dislocations, but with a shear band as the

fundamental slip event. Higher temperatures and strain rates lead to the formation of smoother and more diffuse topographies that exhibit self-affine scaling at small scales. Their rms roughness  $h_{\text{rms}}$  grows roughly as  $h_{\text{rms}} \propto \varepsilon^{1/2}$  at large strain. Our simulations show that the topography is imprinted shortly after yield and is reinforced during subsequent deformation.

To study the emergence of surface roughness, we simulated  $100 \times 100 \times 100$  nm cubes of amorphous  $\text{Cu}_{50}\text{Zr}_{50}$  using molecular dynamics. The initial configuration shown in Fig. 1a, contained  $5.8 \times 10^7$  atoms, interacting with the embedded atom method potential of Cheng & Ma [32]. The initial structure was melt-quenched at a rate of  $10^{11} \text{ K s}^{-1}$ , followed by equilibration for 100 ps at the target temperature and zero pressure. The systems were fully periodic during quench and equilibration, after which we opened the boundaries along the  $z$ -direction, creating two free surfaces. The samples were equilibrated for 100 ps after creating the free surfaces and before compression.

We compressed these samples by dynamically reducing the lengths of the simulation cell in the  $x$ - and  $y$ -directions, keeping the cross-section in the  $xy$ -plane square. We report results in terms of the applied engineering strain  $\varepsilon(t) = 1 - L(t)/L_0$ , where  $L(t)$  is the linear length of the cell (at time  $t$ ), and  $L_0$  the initial initial length. Since a jump in the strain rate generates undesirable shock waves, we gradually increased  $\dot{\varepsilon}(t)$  from zero to a constant value during the first 100 ps of the simulation. We carried out simulations at final strain rates of  $10^7 \text{ s}^{-1}$  and  $10^8 \text{ s}^{-1}$ .

During deformation, we controlled the temperature using a dissipative particle dynamics (DPD) [33] thermostat with a cutoff radius of  $6.5 \text{ \AA}$  – equal to the cutoff radius of the potential – and a damping parameter  $\gamma = 5 \times 10^{-3} \text{ eV ps \AA}^{-2}$ , which leads to a characteristic damping time of approximately 1 ps. Unlike Langevin or Nosé-Hoover thermostats, the Gallilean-invariant DPD thermostat does not overdamp long-wavelength modes, which is important for large-scale simulations such as those reported here.

Plastic deformation roughened the initially flat sample surfaces, which we quantified from a pixel representation  $h_{xy}(\varepsilon)$  of the topography with lateral pixel size  $L_{\text{pix}} \approx 3 \text{ \AA}$ .  $h_{xy}$  is the height of the topmost atom (bottommost for bottom surface) associated with the pixel with center coordinates  $x$  and  $y$ . We performed all statistical analysis on  $h_{xy}$ , e.g., the root-mean-square roughness  $h_{\text{rms}} = \langle h_{xy}^2 \rangle$  where  $\langle \cdot \rangle$  is the average over all pixels. We assume that all heights are leveled such that  $\langle h_{xy} \rangle = 0$ .

Fig. 1b-d show  $h_{xy}$  after 30% compression in our dynamic tests. At the lowest rate and temperature ( $10^7 \text{ s}^{-1}$  and 10 K, Fig. 1b), the most prominent feature is a lentil-shaped dip formed by shear bands. We find a similar topography in a quasistatic simulation, where we imposed compressive strain on the cell in increments of  $\Delta\varepsilon = 10^{-4}$  by affinely remapping all coordinates, followed by subsequent relaxation down to a force of  $10^{-3} \text{ eV \AA}^{-1}$  using the FIRE algorithm [34]. In the other simulations at higher temperature or higher rate, deformation was less localized and the resulting surface topography is more diffuse, see Fig. 1c and d. The roughness amplitude generally decreases with increasing temperature and rate. At  $T = 500 \text{ K}$  and  $\dot{\varepsilon} = 10^8 \text{ s}^{-1}$ , the height range is only 2 nm.

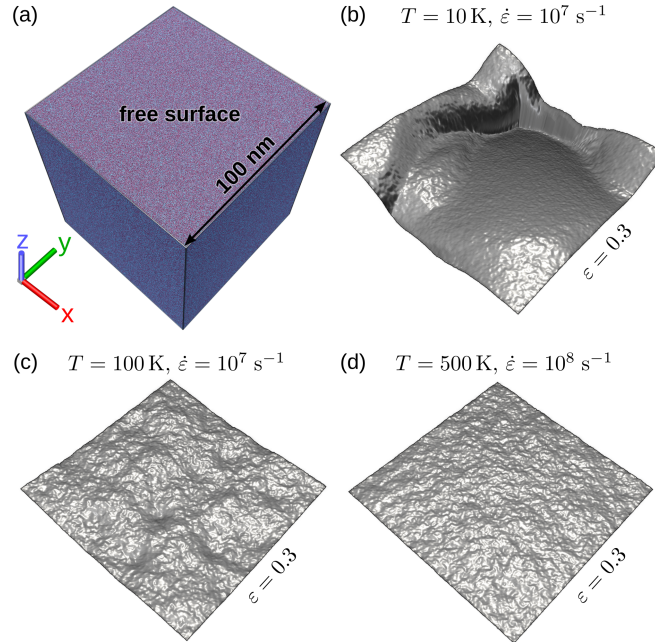


FIG. 1. (a)  $\text{Cu}_{50}\text{Zr}_{50}$  cube with a side length of 100 nm and a free surface in the  $z$ -direction. We simulated biaxial compression along the  $x$ - and  $y$ -directions. (b) Topography of the surface after 30% compression with a rate of  $10^8 \text{ s}^{-1}$  at 10 K. A shear band has formed. No such distinct feature is visible at (c) 100 K and (d) 500 K. The topography becomes smoother with increasing temperature.

Figure 2a shows the mean lateral stress  $(\sigma_{xx} + \sigma_{yy})/2$  as a function of strain  $\varepsilon$ . In most cases, the elastic regime does not end abruptly. After the peak, the stress decreases smoothly, as expected [35–37], and stabilizes at the steady-state flow stress. Increasing temperature and decreasing rate lowers the peak and flow stresses. The only exceptions are

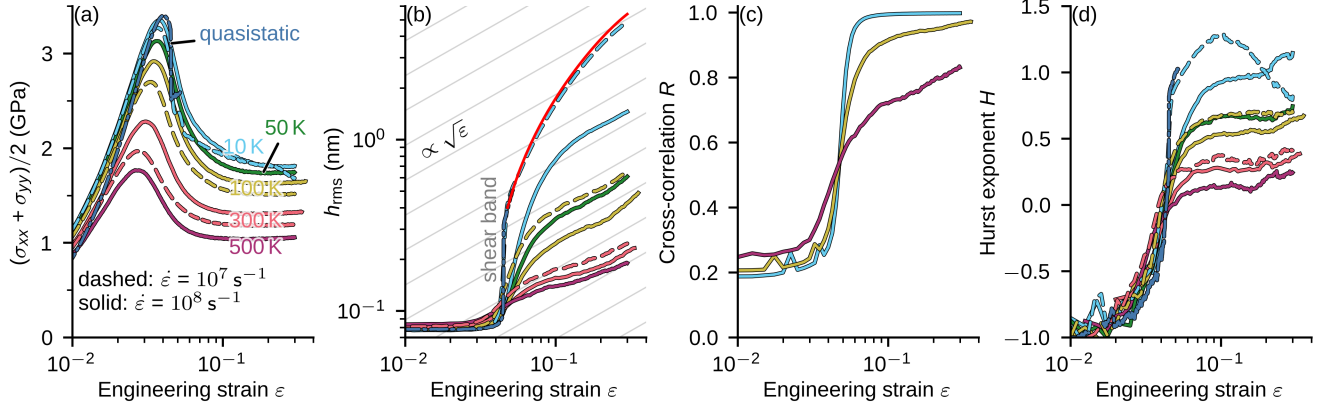


FIG. 2. (a) Lateral normal stress vs. compressive strain  $\epsilon$  in simulations with different strain rates  $\dot{\epsilon}$  and temperatures  $T$ . (b) Root-mean square roughness  $h_{\text{rms}}$ , which increases after yield. A shear band forms in the quasistatic simulation, and in low-rate, low-temperature simulations (here  $\dot{\epsilon} = 10^7 \text{ s}^{-1}$  at 10 K). The thin red line is a model of  $h_{\text{rms}}$  for a topography dominated by a shear band (see text). (c) Cross-correlation  $R$  (see text) between subsequent topographies at intervals of  $\Delta\epsilon \approx 0.0025$ . (d) Hurst exponent extracted from fits to the PSD (see text).

the two simulations with shear banding: the quasistatic test and the dynamic simulation with  $\dot{\epsilon} = 10^7 \text{ s}^{-1}$  at 10 K. In the former case, a sharp stress drop is visible. In the latter case, the stress decreases again close to  $\epsilon = 0.3$ .

In all cases,  $h_{\text{rms}}$  (see Fig. 2b) is initially less than 0.1 nm, as should be expected for an atomically flat surface, but increases after peak stress. The rate of roughening depends on  $\dot{\epsilon}$  and  $T$ . The steepest increase is seen in the quasistatic simulation and the simulation with  $\dot{\epsilon} = 10^7 \text{ s}^{-1}$  at 10 K. Increasing  $\dot{\epsilon}$  and  $T$  leads to a more gradual transition, and lower  $h_{\text{rms}}$  at the same strain. At the highest temperatures, there is little difference between the curves for 300 K and 500 K. At large strain,  $h_{\text{rms}} \propto \epsilon^\alpha$  with  $\alpha \approx 0.5$ , except in the simulation with  $\dot{\epsilon} = 10^7 \text{ s}^{-1}$  at 10 K that forms a shear band.

While  $h_{\text{rms}}$  increases continuously, there is little qualitative difference between the topography formed during yield, and the topography at later stages of deformation. To quantify this observation, we calculated the cross-correlation  $R(\epsilon) = \langle h_{xy}(\epsilon - \Delta\epsilon)h_{xy}(\epsilon) / [h_{\text{rms}}(\epsilon - \Delta\epsilon)h_{\text{rms}}(\epsilon)] \rangle^{1/2}$  between subsequent simulation snapshots with  $\Delta\epsilon = 0.0025$  for the simulations with  $\dot{\epsilon} = 10^8 \text{ s}^{-1}$  (Fig. 2c). Before yield, the cross-correlation is small ( $\approx 0.2$ ), indicating that there are not many common features between subsequent snapshots. This is not surprising, since  $h_{\text{rms}}$  is so low that thermal fluctuations dominate the topography. Af-

ter the peak stress, the cross-correlation increases significantly, with the strongest and most rapid increase seen in the simulation at the lowest temperature of  $T = 10$  K. In this case, the cross-correlation jumps to a value close to one, indicating that the topography is reinforced – peaks grow and valleys become deeper – with little qualitative change. Increasing temperature reduces the correlation, but beyond  $\varepsilon \approx 0.04$ , it stays above 0.5.

In order to examine lateral correlation in the topography, we compute the power-spectral density (PSD),  $C_{q_x q_y}^{2D} = L^{-2} |\tilde{h}_{q_x q_y}|^2$  (or rather its radial average  $C_q^{\text{iso}}$ ), where  $\tilde{h}_{q_x q_y}$  is the discrete Fourier transform of  $h_{xy}$ . (See Ref. [38] for the conventions used here.) If the topography is self-affine with Hurst exponent  $H$ , then the PSD scales as  $C_q^{\text{iso}} \propto q^{-2-2H}$ . Fig. 3a shows how  $C_q^{\text{iso}}$  evolves with strain  $\varepsilon$ . The PSD is constant at small strain, where the residual roughness is given by uncorrelated thermal noise and quenched disorder of the glassy state. At yield,  $C_q^{\text{iso}}$  begins to grow, as can be seen in the curve for  $\varepsilon = 0.04$ , which is just past the peak stress in this simulation. Topographic structure emerges first at small  $q$  or long wavelengths. At a large strain of  $\varepsilon = 0.3$ ,  $C_q^{\text{iso}}$  has a linear region in the double-logarithmic plot, which is the signature of self-affine (scale-free) roughness.

Fig. 3b shows  $C_q^{\text{iso}}$  from the simulations at 100 K, 300 K and 500 K, at  $\varepsilon = 0.3$ . In the double-logarithmic plot, all curves have a linear region at intermediate  $q$ . As a guide to the eye, the gray lines in Figs. 3a and b show ideal fractal scaling with a Hurst exponent  $H = 0.5$ . We extract an estimate for the Hurst exponent from these calculations by fitting the simple model  $C_q^{\text{iso}} = C_{\text{wn}} + C_f q^{-2-2H}$  to the PSD data, excluding data in the long wavelength region  $q < 0.18 \text{ nm}^{-1}$ . The constant  $C_{\text{wn}}$  is a white noise contribution and  $C_f$  the amplitude of the fractal regime.

The individual fits are shown as dashed gray lines in Fig. 3a and b. The combination of white noise and a self-affine regime describe the data well, even at  $\varepsilon = 0.04$  in Fig. 3a where roughening has just begun. The fits now allow us to plot the evolution of  $H$  with strain  $\varepsilon$  (Fig. 2d). There is an initial region of negative  $H$  where the surfaces are flat and do not show self-affine scaling, followed by a jump to a finite value as the surfaces yield.  $H$  depends on temperature and strain rate, with lower temperatures and lower strain rates leading to larger values of  $H$ .

At low temperature and strain rate, the system is near the athermal quasistatic (or overdamped) regime of deformation [39], with the quasistatic simulation as the limiting case. In line with many previous investigations [40, 41], we observe system-spanning shear

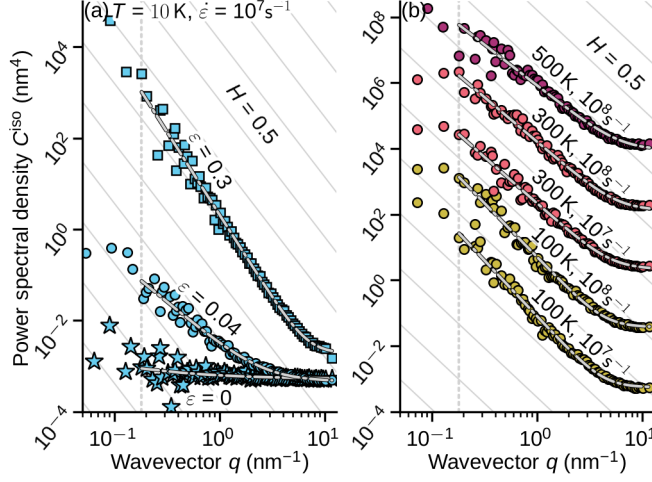


FIG. 3. (a) Radially averaged power spectral density (PSD)  $C_q^{\text{iso}}$  of the surface heights, at three different strains in the simulation with  $T = 10 \text{ K}$  and  $\dot{\epsilon} = 10^7 \text{ s}^{-1}$ . As a consequence of plastic deformation,  $C_q^{\text{iso}}$  increases with strain  $\epsilon$ , first at long wavelengths (small wavevectors  $q$ ). Despite a shear band that forms in this simulation,  $C_q^{\text{iso}}$  is approximately linear in the double logarithmic plot at large  $\epsilon$ . (b)  $C_q^{\text{iso}}$  at  $\epsilon = 0.3$  in simulations at and above 100 K. Gray lines: Fit to a white noise plus power-law model  $C_q^{\text{iso}} = C_{\text{wn}} + C_{\text{f}}q^{-2-2H}$  in the region  $q > 0.18 \text{ nm}^{-1}$ ; the cutoff is indicated by a vertical dashed line. The ordinates in (b) have been shifted for better visibility.

bands that form topography by leaving steps on the surface. The corresponding  $h_{\text{rms}}$ -curve in Fig. 2b can thus be understood using a simple model of the growth of a single surface step described by the function  $h(x) = a(x - L(\epsilon)/2)$ , see Supplemental Material. The result is shown by the red line in Fig. 2b. A random distribution of such steps then leads to a self-affine topography at scales larger than our simulations (see also discussion on dislocations in Ref. [13]).

It is remarkable that the topography appears to be self-affine at large strain (Fig. 3a), even though the overall topography is dominated a single system-spanning shear band. We note that an idealized sawtooth profile (that is *not* self-affine) also exhibits power-law scaling  $C_q^{\text{iso}} \propto q^{-3}$  of the power spectral density – however with a smaller apparent Hurst exponent of  $H = 0.5$ , while our fit of the data in Fig. 3a yields  $H = 0.8$ . Since power-law scaling of  $C_q^{\text{iso}}$  is also plausible in the other simulations with higher rates and temperatures, where no system-spanning shear bands are formed, these shear bands likely do not control the exponent of  $C_q^{\text{iso}}$  in Fig. 3a.

Decreasing either rate or temperature increases both  $h_{\text{rms}}$  and  $H$ . In this respect, the glass is different from metal crystals, where  $h_{\text{rms}}$  and  $H$  due to roughening by plastic deformation are independent of rate and temperature [13]. We note that in particular that the dependence of the scaling exponent  $H$  on rate and temperature is unusual, as scaling exponents in power-law correlated data of phase transitions or critical phenomena are widely regarded as universal [42]. These observations touch upon an ongoing discussion regarding whether the yielding transition (in glassy materials) can be strictly regarded as a phase transition [43–47]. Since our simulations suggest that  $H$  is fixed at yield, the interpretation of yielding as a phase transition may only apply in the athermal case.

The differences between our topographies appear to reflect the temperature and rate sensitivity of plastic flow in the glass. A finite rate and temperature limit the magnitude of plastic events [19, 20]. At fast deformation rates, new events are nucleated before the avalanches triggered by earlier events can finish, and at high temperatures, large avalanches are overwhelmed by thermal noise because of subextensive scaling of the avalanche with system size. This is directly reflected in structural measures of flow. Different scaling relations have been reported for the scaling of a correlation length  $\xi$  between plastic flow events with shear rate  $\dot{\epsilon}$ , such as  $\xi \propto \dot{\epsilon}^{-1}$  (distance  $\xi$  between shear bands in 3D [41]),  $\xi \propto \dot{\epsilon}^{-0.4}$  (characteristic correlation length  $\xi$  in 2D [48]) or  $\xi \propto \dot{\epsilon}^{-0.3}$  (characteristic correlation length  $\xi$  in 3D [48]).

We now attempt a similar scaling collapse of our data for the characteristic length in our system, the height amplitude  $h_{\text{rms}}$ . We attempt to collapse the  $h_{\text{rms}}(\varepsilon)$ -curves from those simulations where no system-spanning shear band is nucleated assuming the empirical relation  $h_{\text{rms}} \propto \dot{\gamma}^\eta T^\kappa$ . Before dividing by  $\dot{\gamma}^\eta T^\kappa$ , we subtracted the small baseline roughness  $h_{\text{rms},0}$  of the undeformed state that reflects thermal fluctuations. We computed  $h_{\text{rms},0}$  as the mean value of  $h_{\text{rms}}(\varepsilon)$  for  $\varepsilon < 0.01$ . Fig. 4 shows the curves after normalization with  $\eta = -0.1$  and  $\kappa = -0.7$ . This choice collapses the data beyond the yield point ( $\varepsilon \gtrsim 0.1$ ).

In summary, the evolution of the surface roughness of a deformed  $\text{Cu}_{50}\text{Zr}_{50}$  metallic glass reflects the dependence of plastic flow on rate  $\dot{\epsilon}$  and temperature  $T$ . At low values of these parameters, the topography is dominated by system-spanning shear bands. At higher temperatures and rates, a more diffuse topography emerges, with some traces of universality: At large strain, the root mean square roughness tends to grow as  $h_{\text{rms}} \propto \varepsilon^\alpha$ , with  $\alpha \approx 0.5$ , and lower values at the highest rates and temperatures. Moreover,  $h_{\text{rms}} \propto \dot{\gamma}^\eta T^\kappa$  at large

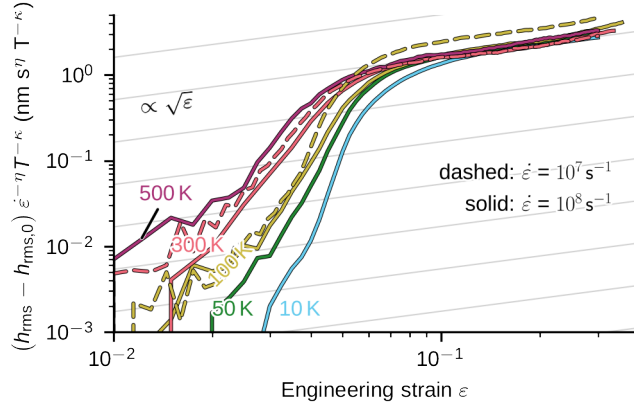


FIG. 4. Root-mean square roughness  $h_{\text{rms}}$ , divided by  $\gamma^\eta T^\kappa$ , with  $\eta = -0.1$  and  $\kappa = -0.7$ . This normalization collapses the  $h_{\text{rms}}$ -curves close at high strain.

strain with  $\eta \approx -0.1$  and  $\kappa \approx -0.7$ . Regardless of rate and temperature, the power-spectral density of all surfaces can be described as the superposition of a self-affine part and constant noise from thermal fluctuations and quenched disorder.

Our results remain valid for small-scale roughness of systems with evolving shear-bands. We note that similar to dislocations [10, 13], a network of shear bands forms a network of steps on a surface, which also carries the signature of self-affine scaling with an exponent that depends on the lateral correlation of these steps. This indicates that during the formation of real-world surfaces, a number of mechanisms may be active at different scales that all lead to self-affine geometries.

*Acknowledgements.* We thank Richard Leute, Gianpiero Moras, Laurent Ponson and Michael Zaiser for useful discussion. We used LAMMPS [49] for all calculations and OVITO PRO [50] and PYVISTA [51] for postprocessing and visualization. Topography data was analyzed with CONTACT.ENGINEERING. We acknowledge support from the European Research Council (StG-757343) and the Deutsche Forschungsgemeinschaft (DFG, grant PA 2023/2). Calculations were carried out at the Jülich Supercomputing Center (JUWELS, grant hka18) and postprocessed at the University of Freiburg (NEMO, DFG grant INST 39/963-1 FUGG). Data is stored on bwSFS (University of Freiburg, DFG grant INST 39/1099-1 FUGG).

[1] M. Urbakh, J. Klafter, D. Gourdon, and J. N. Israelachvili, *Nature* **430**, 525 (2004).

[2] B. N. J. Persson, O. Albohr, U. Tartaglino, A. I. Volokitin, and E. Tosatti, *J. Phys. Condens.*

- Matter **17**, R1 (2005).
- [3] K. N. G. Fuller and D. Tabor, *Proc. R. Soc. Lond. A* **345**, 327 (1975).
  - [4] D. Maugis, *J. Adhes. Sci. Technol.* **10**, 161 (1996).
  - [5] B. N. J. Persson and E. Tosatti, *J. Chem. Phys.* **115**, 5597 (2001).
  - [6] B. N. J. Persson, *Phys. Rev. Lett.* **89**, 245502 (2002).
  - [7] L. Pastewka and M. O. Robbins, *Proc. Natl. Acad. Sci. USA* **111**, 3298 (2014).
  - [8] S. Dalvi, A. Gujrati, S. R. Khanal, L. Pastewka, A. Dhinojwala, and T. D. B. Jacobs, *Proc. Natl. Acad. Sci. USA* **116**, 25484 (2019).
  - [9] Y. Miura, *J. Appl. Phys.* **43**, 2917 (1972).
  - [10] M. Zaiser, F. M. Grasset, V. Koutsos, and E. C. Aifantis, *Phys. Rev. Lett.* **93**, 195507 (2004).
  - [11] J. Gagel, D. Weygand, and P. Gumbsch, *Acta Mater.* **111**, 399 (2016).
  - [12] J. Gagel, D. Weygand, and P. Gumbsch, *Acta Mater.* **156**, 215 (2018).
  - [13] A. R. Hinkle, W. G. Nöhring, R. Leute, T. Junge, and L. Pastewka, *Sci. Adv.* **6**, eaax0847 (2020).
  - [14] H. Fossen, *Structural Geology*, 2nd ed. (Cambridge University Press, Cambridge, 2016).
  - [15] F. Spaepen, *Acta Metall.* **25**, 407 (1977).
  - [16] A. S. Argon, *Acta Metall.* **27**, 47 (1979).
  - [17] M. L. Falk and J. S. Langer, *Phys. Rev. E* **57**, 7192 (1998).
  - [18] T. C. Hufnagel, C. A. Schuh, and M. L. Falk, *Acta Mater.* **109**, 375 (2016).
  - [19] A. Lemaître and C. Caroli, *Phys. Rev. Lett.* **103**, 065501 (2009).
  - [20] H. G. E. Hentschel, S. Karmakar, E. Lerner, and I. Procaccia, *Phys. Rev. Lett.* **104**, 025501 (2010).
  - [21] J. Jackle and K. Kawasaki, *J. Phys. Condens. Matter* **7**, 4351 (1995).
  - [22] T. Sarlat, A. Lelarge, E. Søndergård, and D. Vandembroucq, *Eur. Phys. J. B* **54**, 121 (2006).
  - [23] Z. Zhang, S. Ispas, and W. Kob, *Phys. Rev. Lett.* **126**, 066101 (2021).
  - [24] R. S. Sayles and T. R. Thomas, *Nature* **271**, 431 (1978).
  - [25] B. B. Mandelbrot, *The Fractal Geometry of Nature* (W. H. Freeman, 1982).
  - [26] J. J. Mecholsky, D. E. Passoja, and K. S. Feinberg-Ringel, *J. Am. Ceram. Soc.* **72**, 60 (1989), 00290.
  - [27] D. Bonamy, L. Ponson, S. Prades, E. Bouchaud, and C. Guillot, *Phys. Rev. Lett.* **97**, 135504 (2006).

- [28] T. Candela, F. Renard, Y. Klinger, K. Mair, J. Schmittbuhl, and E. E. Brodsky, *J. Geophys. Res. - Solid Earth* **117**, B08409 (2012).
- [29] A. Gujrati, S. R. Khanal, L. Pastewka, and T. D. B. Jacobs, *ACS Appl. Mater. Interfaces* **10**, 29169 (2018).
- [30] E. Milanese, T. Brink, R. Aghababaei, and J.-F. Molinari, *Nat. Comm.* **10**, 1116 (2019).
- [31] R. Vacher and A. S. de Wijn, *Materials* **14**, 7327 (2021).
- [32] Y. Q. Cheng and E. Ma, *Prog. Mater. Sci.* **56**, 379 (2011).
- [33] T. Soddemann, B. Dunweg, and K. Kremer, *Phys. Rev. E* **68**, 46702 (2003).
- [34] E. Bitzek, P. Koskinen, F. Gähler, M. Moseler, and P. Gumbsch, *Phys. Rev. Lett.* **97**, 170201 (2006).
- [35] J. Rottler and M. O. Robbins, *Phys. Rev. E* **68**, 11507 (2003).
- [36] R. Bhowmick, R. Raghavan, K. Chattopadhyay, and U. Ramamurty, *Acta Mater.* **54**, 4221 (2006).
- [37] F. Shimizu, S. Ogata, and J. Li, *Acta Mater.* **54**, 4293 (2006).
- [38] T. D. B. Jacobs, T. Junge, and L. Pastewka, *Surf. Topogr. Metrol. Prop.* **5**, 013001 (2017).
- [39] K. M. Salerno, C. E. Maloney, and M. O. Robbins, *Phys. Rev. Lett.* **109**, 105703 (2012).
- [40] K. Albe, Y. Ritter, and D. Şopu, *Mech. Mater.* **67**, 94 (2013).
- [41] M. Singh, M. Ozawa, and L. Berthier, *Phys. Rev. Mater.* **4**, 025603 (2020).
- [42] H. E. Stanley, *Rev. Mod. Phys.* **71**, S358 (1999).
- [43] P. K. Jaiswal, I. Procaccia, C. Rainone, and M. Singh, *Phys. Rev. Lett.* **116**, 085501 (2016).
- [44] G. Parisi, I. Procaccia, C. Rainone, and M. Singh, *Proc. Natl. Acad. Sci. USA* **114**, 5577 (2017).
- [45] M. Ozawa, L. Berthier, G. Biroli, A. Rosso, and G. Tarjus, *Proc. Natl. Acad. Sci. USA* **115**, 6656 (2018).
- [46] R. Jana and L. Pastewka, *J. Phys. Mater.* **2**, 045006 (2019).
- [47] M. Ozawa, L. Berthier, G. Biroli, and G. Tarjus, *Phys. Rev. Res.* **2**, 023203 (2020).
- [48] J. T. Clemmer, K. M. Salerno, and M. O. Robbins, *Phys. Rev. E* **103**, 042605 (2021).
- [49] S. Plimpton, *J. Comput. Phys.* **117**, 1 (1995).
- [50] A. Stukowski, *Modell. Simul. Mater. Sci. Eng.* **18**, 015012 (2010).
- [51] C. B. Sullivan and A. Kaszynski, *J. Open Source Softw.* **4**, 1450 (2019).

# Supplemental Material for

## “Nonequilibrium plastic roughening of metallic glasses yields self-affine topographies with strain-rate and temperature-dependent scaling exponents”

### $h_{\text{rms}}$ OF A SURFACE WITH A STEP FORMED BY A SHEAR BAND

In Fig. 2(b), the curve for  $T = 10$  K and  $\dot{\varepsilon} = 10^7 \text{ s}^{-1}$  does not scale  $\propto \varepsilon^{0.5}$  at large strain. Shear bands are formed in this simulation, and the distinct  $h_{\text{rms}}$ -curve can be described using a simple model of the growth of a surface step generated by such a band.

Consider a line scan along the  $x$ -direction and assume that the height profile created by the band can be described as

$$h(x) = a \left( x - \frac{L(\varepsilon)}{2} \right), \quad (\text{S-1})$$

where the dimensionless parameter  $a$  describes the height of the step. The mean height is zero, hence the  $h_{\text{rms}} = L^{-1} \int_0^L h^2(x) dx = aL/\sqrt{12}$ . The length decreases with strain as  $L(\varepsilon) = (1 - \varepsilon) L_0$ . We assume that the step height is a linear function of strain, i.e.

$$a(\varepsilon) = A(\varepsilon - \varepsilon_b) + B, \quad (\text{S-2})$$

where  $A$  and  $B$  are constants, and  $\varepsilon_y$  is the strain at which the band is formed. In reality, the band forms over a range of strain. However, this range is narrow, as can be seen in Fig. 2(b), hence  $\varepsilon_b$  is a good approximation. In Fig. 2(b)  $\varepsilon_b \approx 4.8 \times 10^{-2}$ . At  $\varepsilon_b$ ,  $h_{\text{rms}}$  jumps to a base value  $h_{\text{rms}}(\varepsilon_b) \equiv h_b \approx 4$  nm, which determines  $B$ . By plugging  $L(\varepsilon_b)$  and  $a(\varepsilon_b)$  into the formula for  $h_{\text{rms}}$ , we obtain  $B = h_b\sqrt{12}/((1 - \varepsilon_b) L_0)$ , hence

$$h_{\text{rms}}(\varepsilon) = \frac{L_0}{\sqrt{12}} \left( A(\varepsilon - \varepsilon_b) + \frac{h_b\sqrt{12}}{(1 - \varepsilon_b) L_0} \right) (1 - \varepsilon). \quad (\text{S-3})$$

With  $A = 1$ , we obtain the red curve in Fig. 2(b), which is close to the data for  $\dot{\varepsilon} = 1 \times 10^7 \text{ s}^{-1}$  and  $T = 10$  K.